LASER & PHOTONICS REVIEWS

www.lpr-journal.org

Van der Waals Layered Mineral Getchellite with Anisotropic Linear and Nonlinear Optical Responses

Ravi P. N. Tripathi, Xiaodong Yang, and Jie Gao**

Ultrathin ternary 2D materials have recently gained significant attention in the context of tailoring physical properties of materials via stoichiometric variation, which are crucial to many applications in optoelectronics, thermoelectrics, and nanophotonics. Herein, sulfide mineral getchellite is identified as a new type of ternary layered material and large-area getchellite thin flakes are prepared through mechanical exfoliation. The highly anisotropic linear and nonlinear optical responses of getchellite thin flakes facilitated by the reduced in-plane crystal symmetry are reported, including anisotropic Raman scattering, wavelength-dependent linear dichroism transition, and anisotropic third-harmonic generation (THG). Furthermore, the third-order nonlinear susceptibility for getchellite crystal is retrieved from the thickness-dependent THG emission. The demonstrated strong anisotropic linear and nonlinear optical properties of van der Waals layered getchellite will have implications for future technological innovations in photodetectors, optical sensors, nonlinear optical signal processors, and other on-chip photonic device prototypes.

1. Introduction

Van der Waals (vdW) nanomaterials with their exceptional physical properties such as quantum confinement, interlayer coupling, dangling-bond-free smooth surface,[1] superior electronic response, and anisotropic optical response[2] have paved an effective way to tailoring light-matter interactions beyond the subwavelength scale. Since the successful exfoliation of 2D vdW nanomaterials in 2004,[3] significant efforts have been dedicated to unveiling their full potential in advancing many research fields[4] especially condensed matter physics,[5] electronics,[6] energy storage,[7] sensing,[8] and quantum photonics.[9] Despite the progress so far, the library of the explored 2D vdW nanomaterials is typically confined to mono-elemental and binary materials[2,10] such as black phosphorous, tellurium, GeS, GeSe, GeAs, ReS_2, and transition metal dichalcogenides (TMDs).[11] Recently, complex 2D vdW nanomaterials have emerged with unique physical properties[12] which are not exhibited for the mono-elemental and binary layered vdW material systems such as extraordinary charge carrier mobility, favorable band structure,[13] and phonon vibration.[12–14] Moreover, introducing novel multi-elemental layered vdW materials[15] into optoelectronic and photonic devices will allow the increased adaptability and versatility for the relevant applications.[15,16]

In this regard, ternary layered vdW materials such as Ta_2NiS_5, Bi_2O_2Se, and other ternary TMDs have recently gained substantial attention.[11,12,14,17] Considerable efforts have been shown in exploring ternary vdW materials as novel 2D platforms used for a variety of applications ranging from electronic transport to energy storage.[11,12,14,18] Chromium-based layered materials (CrO*X*, *X* = Cl and Br; $Cr_2Ge_2Te_6$) have been demonstrated as intrinsic ferromagnet,[19] whereas bismuth based ternary materials (Bi_2O_2Se; BiO*X*, *X* = Cl and Br) have been explored to investigate spin-orbit coupling and magneto-transportation.[12,14,20] Also, other associated derivatives have been demonstrated for efficient phototransistors, memristors, and electronic devices. Recently, the attention has been dedicated for tailoring light-matter interactions in such ternary layered vdW materials, for example, Ta_2NiS_5 nanosheets for broadband optical pulse generation and ultrafast photonics,[17] Cr_2NO_2 for spin filtering,[21] and BiOCl as ultraviolet (UV) photodetectors.[22] Nevertheless, the understanding of ternary layered vdW materials is in its early stages and a considerable amount of work is yet to be done for the comprehensive analysis of such promising material systems as well as the further expansion of the current existing 2D materials library.

From another perspective, there has been a recent trend in 2D materials research about the exploration of complex naturally occurring layered minerals,[16] which have facilitated a unique opportunity to advance various important applications and phenomena such as electrocatalysts, thermoelectrics, supercapacitors, topological insulators, high electrical conductivity, and optoelectronic integration. For example, strong vibrational and mechanical anisotropy of the exfoliated layered orpiment (As_2S_3) has been demonstrated.[23] Also, the layered franckeite ($Pb_5Sn_2FeSb_2S_{14}$) has been studied for the application in near-infrared photodetection and the anisotropic nonlinear optical responses.[24,25] The exfoliated cylindrite ($Pb_3Sn_4FeSb_2S_{14}$)

R. P. N. Tripathi, X. Yang, J. Gao
Department of Mechanical and Aerospace Engineering
Missouri University of Science and Technology
Rolla, MO 65409, USA
E-mail: yangxia@mst.edu; gaojie@mst.edu

The ORCID identification number(s) for the author(s) of this article can be found under https://doi.org/10.1002/lpor.202100182

DOI: 10.1002/lpor.202100182

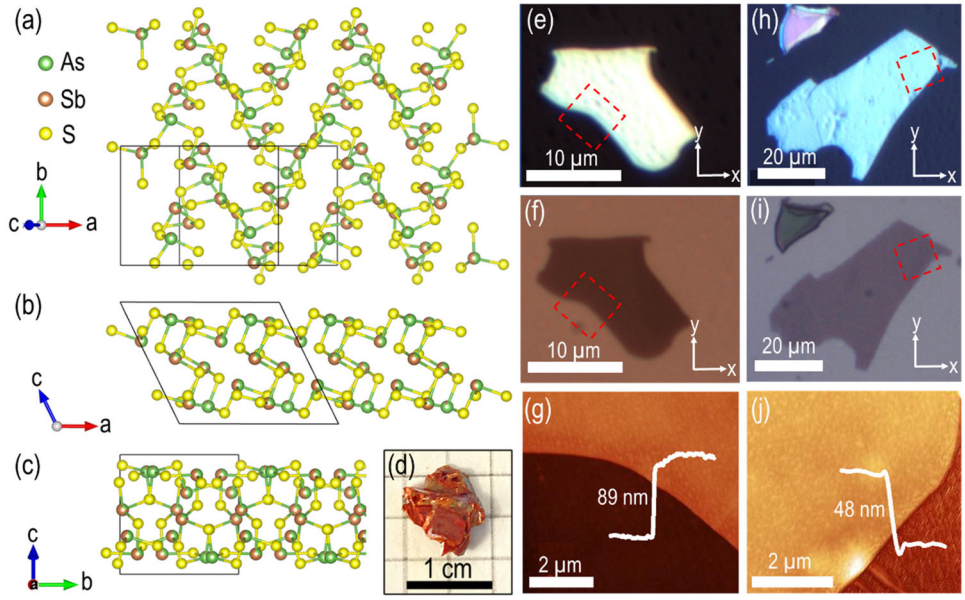

Figure 1. Getchellite crystal structure and exfoliated thin flakes. a–c) Schematic representation of getchellite crystal structure from three side views. d) Image of typical bulk natural getchellite mineral (size: 1 cm × 1 cm). e,h) Optical reflection microscopic images and f,i) optical transmission microscopic images of mechanically exfoliated getchellite thin flakes on glass substrate, respectively. Red dashed-line box indicates the scanned region for AFM image, whereas *x*-axis and *y*-axis signify the crystal's *a*-axis and *b*-axis, respectively. g) and j) AFM images of the marked regions in the reflection and transmission microscope images. The line profiles signify the thickness and smoothness of the investigated flake region.

nanosheets have been shown to preserve the intrinsic magnetic interactions.[26] In addition, the exfoliated teallite ($PbSnS_2$) flakes have been applied in electrocatalytic energy reactions and anisotropic optoelectronics.[27,28] The layered kawazulite (Bi_2Te_2Se) have been identified as a naturally occurring topological insulator.[29]

Motivated by this, herein we identify getchellite as a new type of anisotropic ternary layered vdW material. Getchellite is a rare sulfide mineral of arsenic and antimony with the chemical formula of $AsSbS_3$, which was discovered by B. G. Weissberg from an epithermal arsenical gold deposit at the Getchell mine, Nevada, United States.[30] Getchellite shows dark blood-red color and orange-red streak. Getchellite has a Mohs scale hardness of 1.5 to 2 with a perfect cleavage yielding flexible and inelastic lamellae.[30] Recently, transient absorption spectroscopy has been used to reveal the spatiotemporal dynamics of photocarriers in an $AsSbS_3$ flake from a synthetic crystal.[31] However, the linear and nonlinear optical properties of getchellite are still unknown so far. Here, we explore the anisotropic linear and nonlinear optical responses of mechanically exfoliated getchellite thin flakes. It is shown that natural mineral getchellite can be mechanically exfoliated into ultrathin flakes. We further use high-resolution transmission electron microscopy (HRTEM) and energy dispersive X-ray spectroscopy (EDXS) techniques to determine the crystal structure and chemical composition of getchellite crystal. Subsequently, anisotropic Raman vibrational modes in getchellite thin flakes are investigated using angle-resolved polarized Raman spectroscopy. The polarization and wavelength-dependent linear dichroism transition effects from getchellite thin flakes are also observed with optical absorption spectroscopy. Furthermore, the anisotropic THG response of getchellite crystal with respect to the incident linear polarization of pump beam is probed and the third-order nonlinear susceptibility is retrieved from the thickness-dependent THG emission. These results will provide new opportunities for advancing future photonic and optoelectronic applications in photodetectors, optical sensors, nonlinear optical signal processors, and integrated photonic circuits.

2. Results and Discussion

2.1. Structural and Chemical Composition Analysis of Getchellite Crystal

Getchellite is a natural, thermodynamically-stable, and mixed-metal sulfide mineral composed of arsenic (As), antimony (Sb), and sulfur (S). It has a monoclinic crystal structure belonging to the $P2_1/a$ space group with the unit cell parameters of $a = 11.85$ Å, $b = 8.99$ Å, $c = 10.16$ Å, and $\beta = 116.45°$. **Figure 1**a-c schematically depicts the atomic arrangement in a typical getchellite crystal from three side views. The structure is made up of the puckered M_8S_8 ring (M = As, Sb) connected to each other by bridging additional sulfur atoms to form sheets parallel to (001).[30,32] The angle of S—M—S and M—S—M have been estimated as ≈96.1° and 101.2°.[33] These atomic sheets are further stacked with each other via weak vdW forces, which makes mechanical exfoliation feasible from the bulk crystal. Within the atomic sheet, all metal sites are three-coordinated by S, with the MS_3 unit forming trigonal pyramids. The M—S bond distance in MS_3 pyramids ranges in between 2.275 to 2.489 Å.[30,32,33]

The bulk natural getchellite mineral (from Twin Creeks mine, Potosi District, Humboldt County, Nevada, United States) as shown in Figure 1d is mechanically exfoliated with Nitto tape (SPV 224) to obtain thin flakes of several thicknesses on glass substrate. Optical reflection and transmission microscope im-

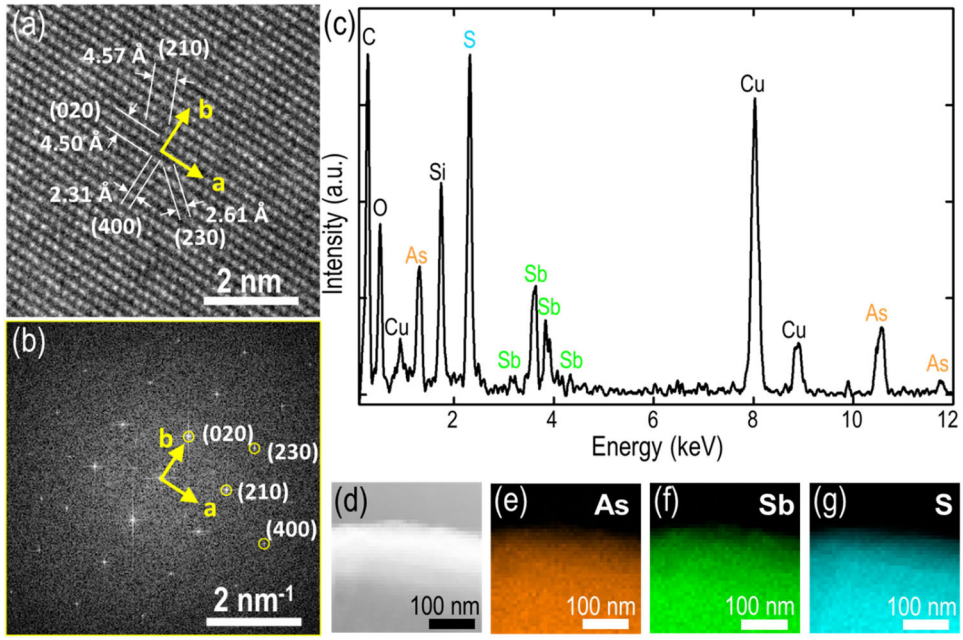

Figure 2. TEM and TEM-EDXS mapping of getchellite crystal. a) Representative atomic HRTEM image of an ultrathin getchellite flake. b) FFT of (a) showing the reflections of the crystal lattice. c) Average EDXS spectrum. The peaks of three major elements As, Sb, and S are primarily considered for elemental quantification of the probed getchellite crystal. d) Dark-field TEM image of the probed region. e–g) TEM-EDXS mapping of getchellite crystal showing the presence of As, Sb, and S, respectively.

ages of one prepared getchellite flake are shown in Figures 1e and 1f, which also underline the high aspect ratio of lateral dimension (≈18 µm) and thickness (≈89 nm) for the flake. In addition, the high aspect ratio is also noticed in another exfoliated flake, as shown in Figure 1h,i. To further ensure this, a section of the prepared flake indicated by the red dashed-line box is scanned using atomic force microscopy (AFM) to estimate the flake thickness and surface smoothness. The obtained AFM images are shown in Figure 1e,j, giving the flake thicknesses of 89 and 48 nm. Furthermore, the getchellite crystal is characterized using HRTEM and EDXS to determine the atomic arrangement and chemical composition. **Figure 2**a shows a HRTEM image of getchellite crystal with the determined lattice spacings of ≈4.50 and ≈2.31 Å and the intersection angle of ≈89°, which are consistent with the [020] and [400] sets of planes for the monoclinic crystal. Figure 2b presents the indexed fast Fourier transform (FFT) of the HRTEM image of Figure 2a, where the reflections of the crystal lattice are marked. Next, the chemical composition of getchellite crystal is quantified. Figure 2c shows the average EDXS spectrum and Figure 2d–g shows the dark-field TEM image of the scanned region and the corresponding TEM-EDXS elemental maps, emphasizing that arsenic (As), antimony (Sb), and sulfur (S) are the prime components which are homogenously distributed in getchellite crystal. The observed copper (Cu) peaks in the EDXS spectrum come from the TEM grid. The elemental composition summarized in **Table 1** is used for the compositional stoichiometry analysis, resulting in an empirical formula of $As_{1.64}Sb_{0.90}S_{3.00}$. The empirical formula determined from EDXS is not completely matched with the generic getchellite chemical formula $As_{0.98}Sb_{1.01}S_3$.[30,33] This deviation between these two formulas can be attributed to the geological origins[27]

Table 1. EDXS quantification of bulk getchellite.

Elements	Concentration (at%)
As	29.64 ± 5.46
Sb	16.19 ± 3.77
S	54.17 ± 8.29

and the presence of carbon (C), oxygen (O), and silicon (Si) impurities in naturally occurring minerals. Such type of deviation between empirical and generic formula has been noticed in other natural vdW materials as well.[27,34]

2.2. Raman Spectroscopy Characterization of Getchellite Crystal

To understand the vibrational modes of getchellite crystal, the Raman spectroscopy is performed on the 89 nm-thick flake in two different polarization configurations. **Figure 3**a shows the measured Raman spectra with a 632.8 nm He—Ne laser as the excitation source in parallel and perpendicular polarization configurations, where the analyzer direction is set to be parallel or perpendicular with respect to the input linear polarization in the signal collection path. The Raman spectrum exhibits several peaks between 70 to 400 cm^{-1}, which are indicated at 83, 132, 152, 167, 181, 269, 285, 297, 327, and 342 cm^{-1}. These observed Raman modes can be assigned as per previously studied Raman spectra of the constituent components of orpiment (As_2S_3)[35] and stibnite (Sb_2S_3).[36] The 83 cm^{-1} peak is attributed to the combination of A_g mode of As_2S_3 (70 cm^{-1}) and A_g mode of Sb_2S_3 (73 cm^{-1}). The peak at 132 cm^{-1} and 152 cm^{-1} are

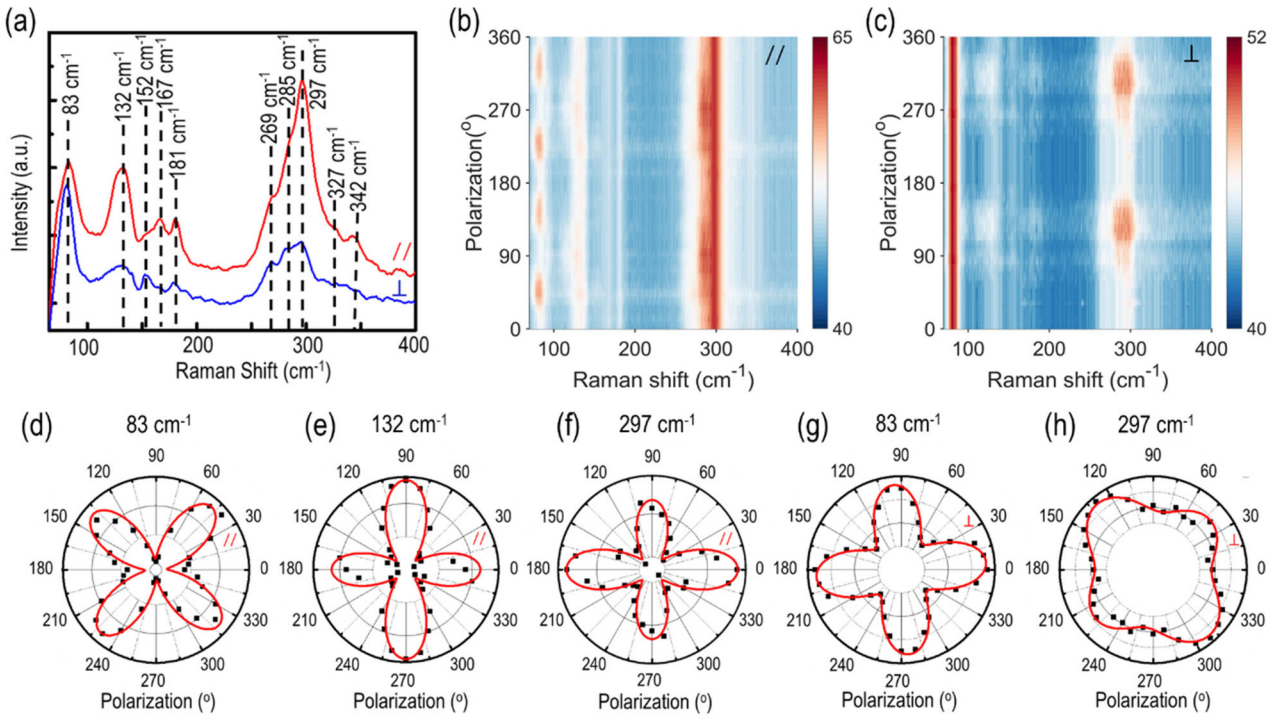

Figure 3. Angle-resolved polarized Raman spectroscopy of getchellite flakes. a) Raman spectra from a typical getchellite flake with 89 nm thickness in parallel (red curve) and perpendicular (blue curve) polarization configurations. The observed Raman peaks are denoted with black dashed lines. b,c) Color maps of angle-resolved polarized Raman spectra in parallel (//) and perpendicular (⊥) polarization configurations. d–h) Polar plots for different Raman modes in parallel configuration at 83, 132, and 297 cm^{-1}, and in perpendicular configuration at 83 and 297 cm^{-1}, respectively. Black squares denote the measured data points and red solid lines are the theoretical fits.

related to A_g modes of As_2S_3 at 137 and 154 cm^{-1}. The 167 and 181 cm^{-1} peaks are assigned as A_g modes of Sb_2S_3 at 156 and 191 cm^{-1}. The peak at 269 and 285 cm^{-1} are ascribed to A_g mode of Sb_2S_3 (283 cm^{-1}). The characteristic 297 cm^{-1} peak is accredited to A_g mode of As_2S_3 (309 cm^{-1}). The last two peaks at 327 and 342 cm^{-1} are attributed to A_g modes of Sb_2S_3 (313 cm^{-1}) and As_2S_3 (354 cm^{-1}), respectively. Importantly, a majority of the Raman modes are present in both polarization configurations. However, the Raman intensity is higher in the case of parallel polarization configuration, indicating that the observed Raman modes are highly polarized.

To better understand the nature of anisotropic optical properties of getchellite crystal, the dependence of the Raman scattering features on the incident linear polarization angles is systematically studied. Getchellite crystal belongs to the monoclinic crystal family. Considering the crystal symmetry as per reported literature, the Raman tensor for different A_g and B_g modes can be written as:[37]

$$R\left(A_g\right) = \begin{bmatrix} ae^{i\emptyset_a} & 0 & de^{i\emptyset_d} \\ 0 & be^{i\emptyset_b} & 0 \\ de^{i\emptyset_d} & 0 & ce^{i\emptyset_c} \end{bmatrix} \quad (1)$$

$$R\left(B_g\right) = \begin{bmatrix} 0 & ee^{i\emptyset_e} & 0 \\ ee^{i\emptyset_e} & 0 & fe^{i\emptyset_f} \\ 0 & fe^{i\emptyset_f} & 0 \end{bmatrix} \quad (2)$$

where a, b, c, d, e, and f are the amplitudes of Raman tensor elements, and $\emptyset_a$, $\emptyset_b$, $\emptyset_c$, $\emptyset_d$, $\emptyset_e$, and $\emptyset_f$ denote the associated phases. For a Raman mode, the observed Raman intensity is strongly related with the Raman tensor and the incident/scattered beam polarization vector. In general, the intensity of Raman mode can be expressed as:

$$I \propto \left|e_i.R.e_s\right|^2 \quad (3)$$

where e_i and e_s denote the unit polarization vectors for the incident and scattered light, R is the Raman tensor of the crystal. In accordance with the experimental configuration, there is no contribution from z-axis, hence the unit polarization vectors are $e_i = (\cos\theta, \sin\theta, 0)$, whereas $e_s = (\cos\theta, \sin\theta, 0)$ and $(-\sin\theta, \cos\theta, 0)$ for parallel and perpendicular polarization configurations, respectively. The resultant Raman intensity for A_g and B_g modes in parallel and perpendicular configurations can be written as follows:[37]

$$I_{A_g}^{//} \propto \left(|a|\sin^2\theta + |b|\cos\emptyset_{ba}\cos^2\theta\right)^2 + \left(|b|\sin\emptyset_{ba}\cos^2\theta\right)^2 \quad (4)$$

$$I_{A_g}^{\perp} \propto \left[\left(|a| - |b|\cos\emptyset_{ba}\right)^2 + \left(|b|\sin\emptyset_{ba}\right)^2\right](\sin\theta\cos\theta)^2 \quad (5)$$

$$I_{B_g}^{//} \propto |e|^2\sin^2 2\theta \quad (6)$$

$$I_{B_g}^{\perp} \propto |e|^2\cos^2 2\theta \quad (7)$$

where // and ⊥ denote the parallel and perpendicular polarization configurations and $\emptyset_{ba} = \emptyset_b - \emptyset_a$ denote the associated phase difference. Figure 3b,c shows the Raman intensity color maps as a function of the incident linear polarization angle in the parallel and perpendicular polarization configurations for the 89 nm-thick getchellite flake. It is observed that the Raman modes are anisotropic in nature and the Raman intensities vary periodically as a function of the incident linear polarization angle. To get more details regarding the periodicity of Raman modes, experimentally recorded angle-resolved Raman spectra are theoretically fitted using Equations (4)–(7). Figure 3d–f shows the polar plots of the Raman modes at 83, 132, and 297 cm^{-1} in parallel configuration, while Figure 3g–h shows the polar plots at 83 and 297 cm^{-1} in perpendicular configuration. The experimental data are denoted as black squares, whereas the theoretical fitting is shown with red solid lines, indicating a good agreement between experimental observation and theoretical fitting. Under the parallel configuration, the B_g mode at 83 cm^{-1} exhibit the characteristic four-lobe pattern with a period of 90° and the Raman intensity maxima at angles ≈45°, ≈135°, ≈225°, and ≈315° (Figure 3d), whereas the A_g modes at 132 and 297 cm^{-1} show anisotropic four-lobe patterns with the Raman intensity maxima either at 90° and 270° (Figure 3e) or 0° and 180° (Figure 3f). On the other hand, under the perpendicular configuration, the Raman intensity patterns show the anisotropic four-lobe patterns with a period of 90° (Figure 1g,h). However, the B_g mode at 83 cm^{-1} reaches the intensity minima at angles ≈45°, ≈135°, ≈225°, and ≈315°, whereas the A_g mode at 297 cm^{-1} reaches the intensity maxima at 45°, 135°, 225°, and 315°, highlighting the Raman intensity maxima of A_g and B_g modes cannot appear at the same angle in two different polarization configurations. The anisotropic angle-resolved Raman spectra also endorse the presence of linear dichroism in getchellite crystal. Moreover, the orientation of A_g modes in the parallel configuration indicates the crystal axis of the probed getchellite flake.[38] Here, the 0° and 90° directions are identified as the *a*-axis and *b*-axis of getchellite crystal,[39] for further probing the anisotropic linear and nonlinear optical responses of the crystal.[38–40]

2.3. Wavelength-Dependent Linear Dichroism Transition in Getchellite Flake

To obtain further insight regarding the intrinsic linear dichroism that resulted from the reduced in-plane crystal symmetry of getchellite, the optical absorption characteristics in the visible range from 420 to 800 nm are investigated using polarization-resolved optical absorption spectroscopy. First, two getchellite flakes of significantly different thicknesses of 48 and 89 nm are selected to study the effect of flake thickness on the optical response. **Figure 4**a–c shows the measured reflectance (*R*), transmittance (*T*), and absorbance ($A = 1 - R - T$) spectra for these two flakes with the incident linear polarization along *a*-axis of the crystal. It is found that the thick flake of 89 nm has a higher reflectance but a lower transmittance compared to the thin flake of 48 nm. In addition, it is noticed that the reflectance from both flakes gradually decreases before the wavelength ≈520 nm and abruptly drops afterwards, while the transmittance registers a significant increase before 560 nm and a more gradual increase subsequently. Hence, the minimum absorbance is exhibited ≈530 nm for both flakes, as shown in Figure 4c. Such wavelength-dependent reflectance, transmittance, and absorbance play a crucial role in generating an anomalous linear dichroism transition behavior in getchellite crystal. The absorbance peak ≈730 nm corresponds to the optical band gap in getchellite crystal.[31] To further investigate the anisotropic features of optical absorption and the linear dichroism transition phenomena, angle-resolved reflectance, and transmittance and absorbance spectra are systematically measured for the 89 nm-thick getchellite flake, as shown in Figure 4d–f. The linear polarization angle is defined relative to *a*-axis of the crystal (along *x*-axis). Intriguingly, the absorbance spectra at different linear polarization angles from 0° to 180° almost converge around the wavelength of 560 nm and the trend in absorbance on both sides are precisely opposite, where the absorbance gradually decreases in the wavelength range to less than 560 nm but increases afterwards. To get a more intuitive understanding, the polar plots of reflectance, transmittance, and absorbance spectral features as a function of the linear polarization angle with a step of 10° are shown in Figure 4g–l, at two wavelengths of 520 and 650 nm located at different wavelength ranges as marked by the vertical dashed lines in Figure 4d–f. All the experimental data exhibit angle-dependent two-lobe patterns and can be fitted with a sinusoidal function of the form $\alpha(\theta) = \alpha_x \cos^2(\theta) + \alpha_y \sin^2(\theta)$, where α_x and α_y are the magnitudes along *x*-axis and *y*-axis. The obtained reflectance, transmittance, and absorbance anisotropy ratios at 520 nm (650 nm) are $R_x/R_y = 1.02$ (1.05), $T_x/T_y = 0.95$ (0.97), and $A_x/A_y = 1.15$ (0.95), respectively.

It is worth noting that the polar plot of absorbance at 520 nm in Figure 4i is consistent with the observed Raman A_g mode at 297 cm^{-1} in Figure 3f, whereas the polar plot absorbance at 650 nm in Figure 4l is rotated exactly 90° relative to that at 520 nm. From this observation we can infer that getchellite crystal absorbs photon energy anisotropically along the directions of *a*-axis and *b*-axis, and the wavelength-dependent linear dichroism transition behavior is present in the crystal. Such linear dichroism transition effect has been recently observed in few other 2D crystals such as palladium diselenide $PdSe_2$[41] and $BaTiS_3$ perovskite chalcogenide.[42] Owing to the presented insight,[41,42] we attribute such wavelength-dependent linear dichroism polarity in getchellite crystal as a consequence of the strong localization of the absorption peaks along two principal crystal directions in the energy band at different wavelengths. Nevertheless, further investigation is desirable for insightful comprehension regarding this phenomenon in ternary sulfide minerals.

2.4. Anisotropic Optical Refraction of Getchellite Flake

We further investigate the birefringence in the 89 nm-thick getchellite crystal using polarization-resolved optical microscopy. The details about the optical setup are discussed in Experimental Section. The incident light polarization is varied from 0° to 180° under the cross-polarization illumination configuration with a step of 10°. **Figure 5**a shows the transmission optical microscopy image at the incident polarization angle of 45° and 90°. It is indicated that the flake shows a slightly higher brightness when the incident polarization is along the 45° direction, compared to

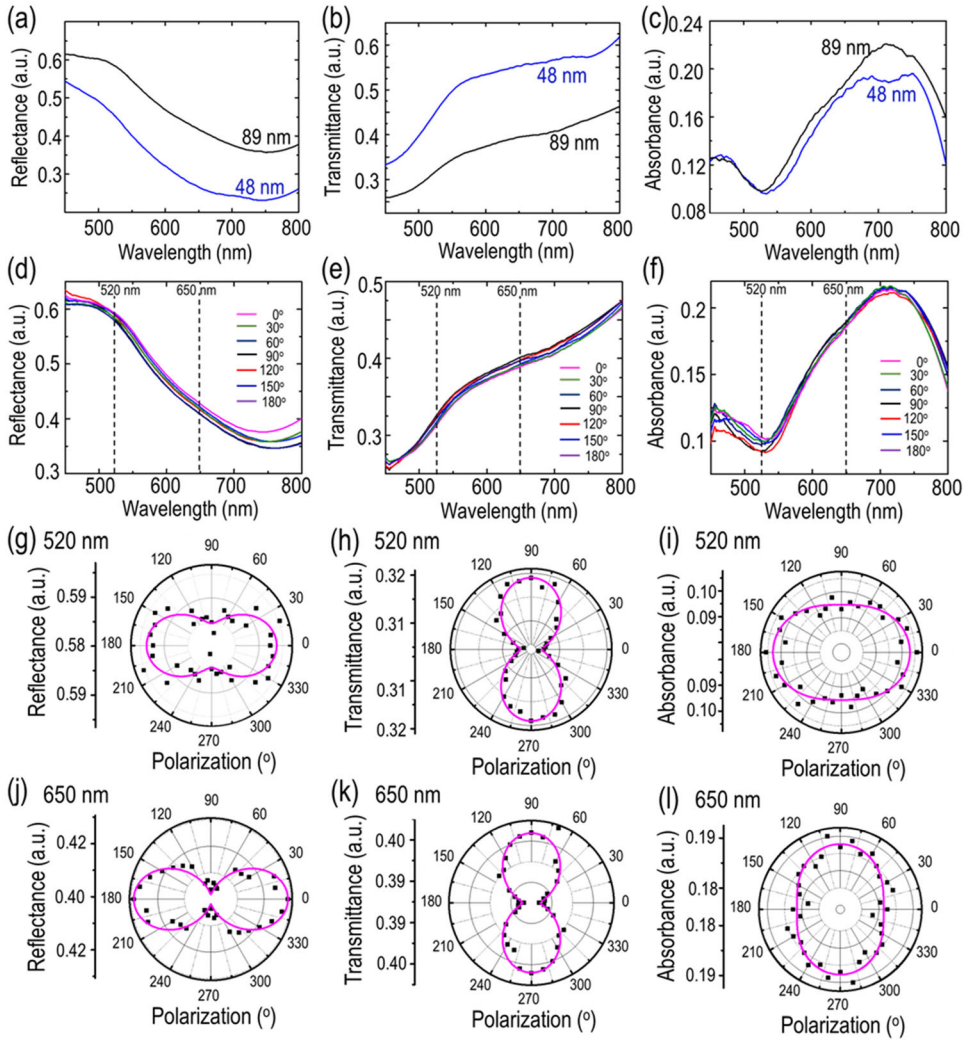

Figure 4. Linear dichroism in getchellite flakes. a–c) Comparison of measured reflectance, transmittance, and absorbance spectra for two getchellite flakes with thicknesses of 48 and 89 nm. Blue solid curves correspond to the 48 nm flake and black solid curves represent the 89 nm flake. d–f) Measured angle-resolved reflectance, transmittance, and absorbance spectra for the 89 nm-thick getchellite flake under incident linear polarization from 0° to 180°. g–l) Evolution of reflectance, transmittance and absorbance as a function of the incident linear polarization angle at two wavelengths of 520 and 650 nm. Black squares represent the experimental data points and magenta solid lines show the fitted curves.

the case when the incident polarization is along the crystalline orientation at 90° (along *y*-axis), due to the birefringence effect of anisotropic getchellite crystal. To further quantify the birefringence, the captured images are processed by normalizing the background intensity and extracting the brightness contrast between the getchellite crystal and the glass substrate. Figure 5b plots the normalized transmitted light intensity from the flake $(I - I_{\min})/(I_{\max} - I_{\min})$ as a function of input linear polarization angle under the cross-polarization illumination configuration. The maximum transmitted light intensity $I_{\max}$ represents the intensity along the 45° direction, while the minimum transmitted light intensity $I_{\min}$ stands for the intensity along the 90° direction. The experimentally extracted values are indicated with black dots, whereas the fitted curve is shown with a solid red curve using the equation $T = \alpha \sin^2(2\theta)$, where α shows the total transmittance along *a*- and *b*-axes. Noticeably, the flake brightness exhibits the characteristic four-lobe pattern with the maxima at angles ≈45° and ≈135°, whereas no brightness contrast is observed at 0° (along *x*-axis) and 90° (along *y*-axis) when the incident polarization is along the crystalline orientation. Such phenomenon of polarization angle-dependent flake brightness emphasizes the presence of birefringence in an anisotropic getchellite crystal. Further, this observation can also be understood in the context of the polarization state of the transmitted light from the getchellite flake.[43,44] When the incident linear polarization is aligned along the crystal axis (*a*- or *b*-axis) of the getchellite flake, the polarization state of the outcoupled light doesn't encounter any change, so that the transmitted light through the flake remains linearly polarized and perpendicular to the analyzer direction in the collection path. Therefore, the brightness contrast of the flake remains low. On the other hand, when the input linear polarization is aligned away from these crystal axes, the transmitted light experiences some amount of phase retardation with the maxima at the incident linear polarization angle of 45° and 135°. This phase

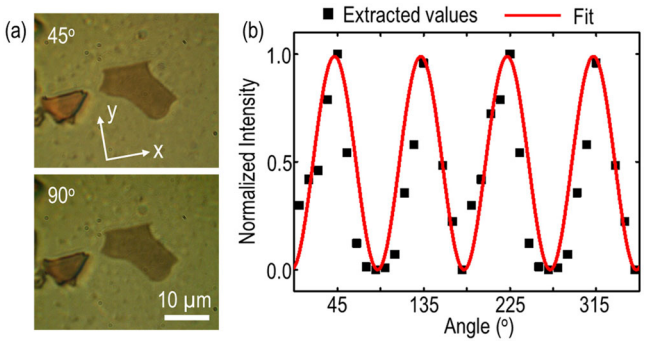

Figure 5. Anisotropic optical refraction of getchellite flake. a) Captured optical images of the 89 nm-thick getchellite crystal in the cross-polarization illumination configuration at two different incident linear polarization angles of 45° and 90°. The camera exposure time is kept same while capturing the images. b) The normalized transmitted light intensity from the flake as a function of the incident linear polarization angle under the cross-polarization illumination configuration.

retardation changes the output polarization state into elliptically polarized light. Consequently, the brightness contrast of the flake systematically varies as a function of the incident polarization angle and reaches the maxima at 45° and 135°.

2.5. Anisotropic THG and Third-Order Nonlinear Susceptibility of Getchellite Crystal

The low in-plane crystal symmetry of getchellite also suggests highly anisotropic nonlinear optical response. The anisotropic THG in getchellite flakes of different thickness is probed by using a 1560 nm pulse laser with a spot size of 1.5 μm. **Figure 6**a shows the recorded THG emission spectrum from the 89 nm-thick getchellite flake, giving the THG emission peak at 520 nm which is one-third of the excitation wavelength. The THG emission process is further confirmed by the cubic power law fitting observed in Figure 6b, where the log-scale plot of the THG emission power as a function of the pump power is presented. Next, the in-plane anisotropic THG emission is studied by measuring the THG intensity dependence on the incident linear polarization of pump beam. The desired linear polarization is obtained by introducing a linear polarizer and a rotating half-wave plate combination in the excitation path. In addition, a linear polarization analyzer is fixed along parallel (0°) and perpendicular (90°) to *a*-axis of the crystal in the collection path for collecting the *x* and *y* components of THG emission. Figure 6c–f shows the measured angular dependence of THG emission power with respect to the incident linear polarization angle for four getchellite flakes of different thicknesses 17, 32, 48, and 89 nm, showing highly anisotropic four-lobe THG patterns for all the flakes. The measured THG emission power includes *x* component (red squares), *y* component (blue dots), and total power (black upper triangles). Noticeably, the maximum THG power is recorded at 0° in the direction of *a*-axis of the crystal (along *x*-axis), whereas the second maximum is obtained at 90° in the direction of *b*-axis (along *y*-axis). The observed anisotropic THG is further corroborated with the theoretical model of the third-order nonlinear susceptibility. For getchellite with the monoclinic crystal structure,[45] the corresponding third-order nonlinear susceptibility tensor can be written as follows:[45,46]

$$\chi^{(3)} = \begin{bmatrix} \chi_{11} & 0 & \chi_{13} & 0 & \chi_{15} & \chi_{16} & \chi_{17} & \chi_{18} & 0 & 0 \\ 0 & \chi_{22} & 0 & \chi_{24} & 0 & 0 & 0 & 0 & \chi_{29} & \chi_{20} \\ \chi_{31} & 0 & \chi_{33} & 0 & \chi_{35} & \chi_{36} & \chi_{37} & \chi_{38} & 0 & 0 \end{bmatrix} \quad (8)$$

where the first term in subscript 1, 2, and 3 denotes *x*, *y*, and *z*, respectively, and the second subscript refers to the combination of three components as:

xxx	*yyy*	*zzz*	*yzz*	*yyz*	*xzz*	*xxz*	*xyy*	*xxy*	*xyz*
1	2	3	4	5	6	7	8	9	0

In accordance with the experimental condition, the getchellite crystal is excited with the linearly polarized electric field of $\vec{E} = \hat{x}\,(|E|\cos\theta) + \hat{y}(|E|\sin\theta)$, where θ is the linear polarization angle relative to *a*-axis of the crystal. As the excitation field polarization always remains in the *x*–*y* plane, the contributions from nonlinear susceptibility tensor containing *z*-component are not accounted for. Thereby, only four non-zero elements χ_{11}, χ_{18}, χ_{22}, and χ_{29} will contribute to the in-plane THG emission process. The electric field components of THG emission and the THG intensity can then be written as:[40]

$$E^{(3\omega)} = \begin{bmatrix} E_x^{(3\omega)} \\ E_y^{(3\omega)} \\ E_z^{(3\omega)} \end{bmatrix} \propto \varepsilon_0 E^3 \begin{bmatrix} \chi_{11}\cos^3\theta + 3\chi_{18}\cos\theta\sin^2\theta \\ \chi_{22}\sin^3\theta + 3\chi_{29}\sin\theta\cos^2\theta \\ 0 \end{bmatrix} \quad (9)$$

$$I_x^{(3\omega)} \propto \left(\chi_{11}\cos^3\theta + 3\chi_{18}\cos\theta\sin^2\theta\right)^2 \quad (10)$$

$$I_y^{(3\omega)} \propto \left(\chi_{22}\sin^3\theta + 3\chi_{29}\sin\theta\cos^2\theta\right)^2 \quad (11)$$

Equations (10) and (11) are used to fit the experimental values in the angular dependence of THG emission. The theoretical fitted curves are shown as the solid curves with the respective colors in Figure 6c–f, showing a good agreement with the measured data.

Additionally, these theoretically fitted curves can be used to retrieve the relative magnitudes of the $\chi^{(3)}$ elements χ_{11}, χ_{18}, χ_{22}, and χ_{29}, which are plotted in **Figure 7**a with respect to the flake thickness. It is shown that the $\chi^{(3)}$ elements are almost unchanged with different flake thicknesses and the average relative magnitudes of $\chi^{(3)}$ elements are $\chi_{11} : \chi_{18} : \chi_{22} : \chi_{29} = 1 : 0.31 : 0.73 : 0.24$, which features the intrinsic nonlinear optical anisotropy in getchellite crystals. Furthermore, the ratio of $|\chi_{11}|^2/|\chi_{22}|^2$ indicates the THG anisotropy ratio $I_x^{(3\omega)}(\theta = 0°)/I_y^{(3\omega)}(\theta = 90°)$ in the getchellite flakes, which almost remains as a constant of 1.88. Next, the third-order nonlinear susceptibility $\chi^{(3)}$ value of getchellite crystals will be estimated. Figure 7b plots for THG emission power as a function of the getchellite flake thickness for the incident linear polarization along *x*-axis. The average pump power is 1.25 mW with 9.82 GW cm^{-2} peak irradiance. The THG emission power gradually increases up to 0.65 pW for the 102 nm-thick getchellite flake and then exponentially decays. The thickness-dependent THG emission response can be understood in terms of the competitive processes of optical gain and loss. For low flake thickness, the

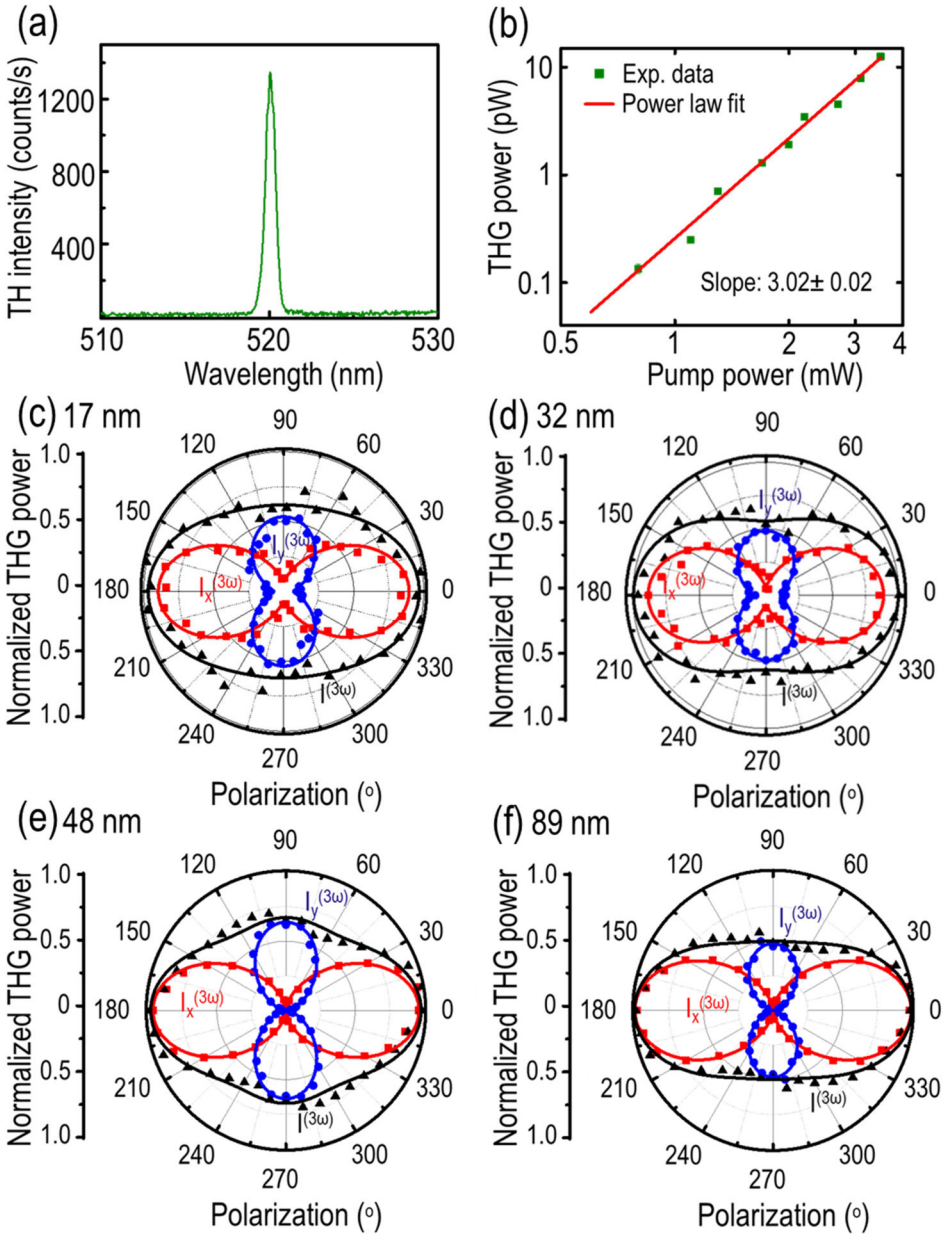

Figure 6. Anisotropic THG emission from getchellite flakes. a) Recorded THG emission spectrum from the 89 nm-thick getchellite flake. b) Logarithmic scale plot of THG power as a function of pump power. Green squares show the measured data points and red solid line is the power law fit. c–f) Polarization-resolved angular dependence of THG emission power for four getchellite flakes with thicknesses of 17, 32, 48, and 89 nm. Red squares, blue dots, and black triangles denote the measured *x*-component ($I_x^{(3\omega)}$), *y*-component ($I_y^{(3\omega)}$), and total ($I^{(3\omega)}$) THG emission power. The theoretical fittings are plotted as solid curves.

THG emission power is proportional to the square of the flake thickness, which is observed in Figure 7b for the flake thickness up to ≈110 nm. As the flake thickness further increases, the strong optical absorption plays a crucial role to attenuate the THG signal propagating through the flake. This trend is observed in the exponential decay of the THG signal for the flake thickness greater than 110 nm. This exponentially attenuated THG signal enables us to extract the imaginary part of the refractive index (k_3) at $\lambda_3 = 520$ nm for getchellite crystal with the fitting of THG emission power $P^{(3\omega)}(l) = \mathrm{A}l^2 \exp(-\frac{4\pi k_3 l}{\lambda_3})$, where A is a constant, and l is the flake thickness. The exponential fitting for THG emission power is plotted in Figure 7b with the fitted k_3 of 0.745. From literature, the real part of the refractive index of getchellite crystal n_3 is ≈2.72.[47] By taking into account the values of refractive index and other experimental parameters of average pump power, laser pulse width, repetition rate, and spot size ($P^{(\omega)}$= 1.25 mW, τ = 90 fs, f_{rep}= 80 MHz, and W = 1.5 μm) at the pump wavelength of 1560 nm, the magnitude of

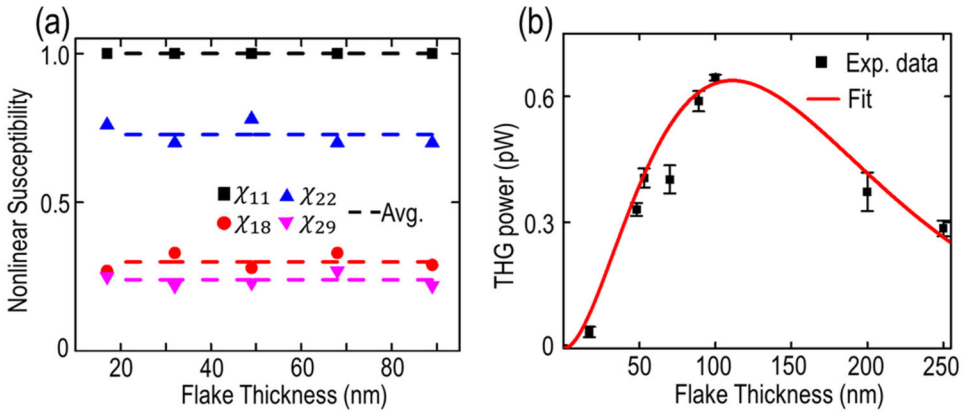

Figure 7. Third-order nonlinear susceptibility and thickness-dependent THG emission. a) Retrieved relative magnitudes of χ_{11}, χ_{18}, χ_{22}, χ_{29} as a function of the flake thickness, as shown with black squares, blue upper triangles, red dots, and magenta lower triangles. The average values are represented with dashed lines in respective colors. b) Thickness-dependent THG emission power. Measured values are shown with black squares with error bars, whereas theoretical fitting is plotted as a red solid curve.

$\chi^{(3)}$ can be estimated by the following expression:[38]

$$P^{(3\omega)}(l) = \frac{9\omega^2 l^2}{16\sqrt{n_3^2 + k_3^2 n_1^3}\,\epsilon_0^2\, c^4}\left|\chi^{(3)}\right|^2 \frac{P^{(\omega)3}}{f_{rep}^2\, W^4 \tau^2 \left[\frac{\pi}{4\ln 2}\right]^3} \times \left(\frac{e^{-\frac{4\pi k_3 l}{\lambda_3}} - 2e^{-\frac{2\pi k_3 l}{\lambda_3}} + 1}{l^2\left(\frac{4\pi^2 k_3^2}{\lambda_3^2}\right)}\right) e^{-\frac{4\pi k_3 l}{\lambda_3}} \quad (12)$$

where n_1 is the real part of the refractive index of getchellite crystal at the fundamental wavelength $\lambda_1 = 1560$ nm and here $n_1 = 2.72$ is used. The estimated magnitude of $\chi^{(3)}$ for getchellite crystal is 2.89×10^{-20} m^2 V^{-2}.

3. Conclusions

In summary, we have prepared large-area getchellite crystal flakes of various thicknesses via mechanical exfoliation method. The crystal structure and chemical composition of getchellite flakes have been extensively characterized. The anisotropic linear and nonlinear optical properties of getchellite thin flakes have been demonstrated, including anisotropic Raman scattering, linear dichroism transition effect, and anisotropic THG response. With angle-resolved polarized Raman spectroscopy, we have shown that the Raman vibrational modes are anisotropic in nature, attributed to the reduced in-plane symmetry in getchellite crystal. Furthermore, by using polarization-resolved optical absorption spectroscopy, we have demonstrated the wavelength-dependent linear dichroism transition effect in getchellite crystal, which has not been explored in naturally occurring ultrathin ternary vdWs crystals. We have also explored anisotropic nonlinear optical response of getchellite crystal in term of the THG emission and extracted the third-order nonlinear susceptibility for getchellite crystal. With this hindsight, we envisage that getchellite will be a valuable addition to expand the current existing layered vdW materials library. Moreover, these promising findings in the context of structural, vibrational, and optical anisotropy for getchellite crystal will be relevant not only to the insightful understanding of other naturally occurring complex vdW materials, but also pave a way of its engagement for polarization-sensitive linear and nonlinear optical devices for future photonic and optoelectronic applications such as photodetection, frequency conversion, wavelength-division multiplexing, encrypted optical signal processing, and optical communication.

Lastly, the uniqueness in the complex crystal structure of ternary getchellite facilitates an exceptional platform to tailor the optical, vibrational, electronic, and mechanical responses towards its binary-element constituent orpiment and stibnite via stoichiometric engineering, which will lead to many other important applications by utilizing this material. The exfoliated getchellite flakes have been studied in the context of photocarrier lifetime, diffusion coefficient, and charge carrier mobility,[31] with the reported values comparable with other vdW materials. These results stimulate its utilization for optoelectronic applications. In addition, getchellite is found to be a direct band gap semiconductor with the value ≈1.74 eV, which is close to an ideal single-junction photovoltaic band gap. Hence, it endorses the prospect of the utilization for photovoltaic and solar cell applications. Furthermore, it would also be interesting to examine getchellite in the context of mechanical properties such as flexibility, strain, and Young's modulus for highly sensitive wearable and flexible device applications. Nevertheless, we anticipate that getchellite and other complex vdW layered minerals certainly have the potentials to meet the increasingly growing demand for the application-based high performance of future nanoscale electronic and optoelectronic devices.

4. Experimental Section

Sample Preparation: Getchellite flakes of various thicknesses were mechanically exfoliated using Nitto tape (SPV 224) from bulk natural getchellite mineral (from Twin Creeks mine, Potosi District, Humboldt County, Nevada, United States). The glass substrates with 1 cm × 1 cm were treated with deionized water, acetone, and isopropanol followed by ultrasonication for 15 min to remove the undesirable residues from the sur-

face. These pretreated glass substrates were further used for transferring the getchellite thin flakes.

Angle-Resolved Polarized Raman Spectroscopy: For collecting the Raman spectra, the sample was excited with a 632.8 nm He—Ne laser using a 40× objective lens (NA = 0.65) and the back-reflected signal was collected via the same objective lens to a spectrometer (Horiba, iHR 520) with a beam splitter. The incident beam polarization was controlled using a linear polarizer and a rotating half-wave plate in the excitation path. To reject the laser light, an edge filter (Semrock, LP02-633RE-25) was introduced in the collection path. The collected signal was further passed through a linear polarization analyzer in the collection path to record the parallel and perpendicular polarization components of the Raman spectra.

Polarization-Resolved Optical Absorption Spectroscopy: For the polarization-resolved optical absorption measurement, a broadband white light source (Thorlabs, SLS201L, 360–2600 nm) was passed through a linear polarizer and a half-wave plate and then focused on the probed getchellite flakes with a 80× objective lens (NA = 0.5). For measuring the reflection spectrum, the back-reflected light was collected from the sample using the same objective lens and routed towards the spectrometer using a beam splitter. Next, the light source spectrum in the reflection configuration was measured by mounting a silver mirror on the sample stage. The reflectance (R) spectrum was then calculated by normalizing the sample response by the light source spectrum. In the case of the transmission spectrum, the transmitted light through the sample was collected using another 100× objective lens (NA = 0.7) and then routed towards the spectrometer. Next, the light source spectrum in the transmission configuration was measured by moving out the sample from the illumination path. The transmittance (T) spectrum was calculated by normalizing the sample response by the light source spectrum. Finally, the absorbance (A) spectrum was obtained by using the relation of $A = 1 - R - T$.

Birefringence Measurement: A broadband white light source was passed through a linear polarizer and focused on the probed getchellite flake with a 20× objective lens (NA = 0.42). The transmitted light was collected with another 20× objective lens (NA = 0.42) from the other side of the substrate and routed to a charge-coupled device (CCD) camera to capture the image. Further, a half-wave plate was engaged to rotate the linear polarization of incident beam from 0° to 180° while maintaining the cross-polarization illumination configuration for each incident linear polarization angle by using a linear polarization analyzer in the collection path. The camera exposure time was kept same during the measurement. The captured images were further processed for filtering out the contribution from the background and extracting the brightness contrast between the getchellite crystal and the glass substrate. Finally, the normalized transmitted light intensity from the flake was plotted as a function of the incident polarization angle to examine the birefringence of the crystal.

THG Emission Measurement: For collecting the THG emission, the sample was pumped with a femtosecond laser source at the wavelength of 1560 nm (pulse width 90 fs, repetition rate 80 MHz) using a 40× objective lens (NA = 0.65). The transmitted THG signal was collected through a 100× objective lens (NA = 0.7). The incident pump beam was filtered out by putting a shortpass filter in the collection path. The THG signal was then routed to a spectrometer and an imaging camera for collecting the spectra and corresponding image.

Acknowledgements

The authors acknowledge support from the National Science Foundation under Grant No. ECCS-1653032 and DMR-1552871. The authors also thank Shatadru Chakravarty and Eric Bohannan for their help in acquiring the TEM and AFM data.

Conflict of Interest

The authors declare no conflict of interest.

Data Availability Statement

Research data are not shared.

Keywords

getchellite, linear dichroism transition, optical anisotropy, ternary 2D materials, third-harmonic generation

Received: April 2, 2021
Revised: August 31, 2021
Published online:

[1] F. Xia, H. Wang, D. Xiao, M. Dubey, A. Ramasubramaniam, *Nat. Photonics* **2014**, *8*, 899.
[2] C. Wang, G. Zhang, S. Huang, Y. Xie, H. Yan, *Adv. Opt. Mater.* **2020**, *8*, 1900996.
[3] K. S. Novoselov, A. K. Geim, S. V. Morozov, D. Jiang, Y. Zhang, S. V. Dubonos, I. V. Grigorieva, A. A. Firsov, *Science* **2004**, *306*, 666.
[4] D. Chi, K. J. Goh, A. T. Wee, *2D Semiconductor Materials and Devices*, Elsevier, New York **2019**.
[5] N. Samarth, *Nature* **2017**, *546*, 216.
[6] G. Fiori, F. Bonaccorso, G. Iannaccone, T. Palacios, D. Neumaier, A. Seabaugh, S. K. Banerjee, L. Colombo, *Nat. Nanotechnol.* **2014**, *9*, 768.
[7] X. Zhang, L. Hou, A. Ciesielski, P. Samorì, *Adv. Energy Mater.* **2016**, *6*, 1600671.
[8] S. Yang, C. Jiang, S.-h. Wei, *Appl. Phys. Rev.* **2017**, *4*, 021304.
[9] A. Reserbat-Plantey, I. Epstein, I. Torre, A. T. Costa, P. Gonçalves, N. A. Mortensen, M. Polini, J. C. Song, N. M. Peres, F. H. Koppens, *ACS Photonics* **2021**, *8*, 85.
[10] P. Miró, M. Audiffred, T. Heine, *Chem. Soc. Rev.* **2014**, *43*, 6537.
[11] W. Gao, Z. Zheng, P. Wen, N. Huo, J. Li, *Nanophotonics* **2020**, *9*, 2147.
[12] T. Gao, Q. Zhang, L. Li, X. Zhou, L. Li, H. Li, T. Zhai, *Adv. Opt. Mater.* **2018**, *6*, 1800058.
[13] F. Cui, Q. Feng, J. Hong, R. Wang, Y. Bai, X. Li, D. Liu, Y. Zhou, X. Liang, X. He, *Adv. Mater.* **2017**, *29*, 1705015.
[14] L. Wang, P. Hu, Y. Long, Z. Liu, X. He, *J. Mater. Chem. A* **2017**, *5*, 22855.
[15] X. Duan, C. Wang, Z. Fan, G. Hao, L. Kou, U. Halim, H. Li, X. Wu, Y. Wang, J. Jiang, *Nano Lett.* **2016**, *16*, 264.
[16] R. Frisenda, Y. Niu, P. Gant, M. Muñoz, A. Castellanos-Gomez, *npj 2D Mater. Appl.* **2020**, *4*, 38.
[17] M. Ma, J. Zhang, Y. Zhang, X. Wang, J. Wang, P. Yu, Z. Liu, Z. Wei, *Nanophotonics* **2020**, *9*, 2341.
[18] Y. Hao, A. Huang, S. Han, H. Huang, J. Song, X. Sun, Z. Wang, L. Li, F. Hu, J. Xue, S. Peng, *ACS Appl. Mater. Interfaces* **2020**, *12*, 29393.
[19] C. Gong, L. Li, Z. Li, H. Ji, A. Stern, Y. Xia, T. Cao, W. Bao, C. Wang, Y. Wang, *Nature* **2017**, *546*, 265.
[20] M. Meng, S. Huang, C. Tan, J. Wu, Y. Jing, H. Peng, H. Xu, *Nanoscale* **2018**, *10*, 2704.
[21] J. Yang, S. Zhang, L. Li, A. Wang, Z. Zhong, L. Chen, *Matter* **2019**, *1*, 1304.
[22] M. Li, J. Zhang, H. Gao, F. Li, S.-E. Lindquist, N. Wu, R. Wang, *ACS Appl. Mater. Interfaces* **2016**, *8*, 6662.
[23] M. Siškins, M. Lee, F. Alijani, M. R. Van Blankenstein, D. Davidovikj, H. S. Van Der Zant, P. G. Steeneken, *ACS Nano* **2019**, *13*, 10845.
[24] A. J. Molina-Mendoza, E. Giovanelli, W. S. Paz, M. A. Niño, J. O. Island, C. Evangeli, L. Aballe, M. Foerster, H. S. Van Der Zant, G. Rubio-Bollinger, *Nat. Commun.* **2017**, *8*, 14409.
[25] R. P. Tripathi, J. Gao, X. Yang, *Sci. Rep.* **2021**, *11*, 8510.

[26] Y. Niu, J. Villalva, R. Frisenda, G. Sanchez-Santolino, L. Ruiz-González, E. M. Pérez, M. García-Hernández, E. Burzurí, A. Castellanos-Gomez, *2D Mater.* **2019**, *6*, 035023.
[27] R. Gusmão, Z. Sofer, J. Luxa, M. Pumera, *J. Mater. Chem. A* **2018**, *6*, 16590.
[28] Z. Shu, Q. Peng, P. Huang, Z. Xu, A. A. Suleiman, X. Zhang, X. Bai, X. Zhou, T. Zhai, *Matter* **2020**, *2*, 977.
[29] P. Gehring, H. M. Benia, Y. Weng, R. Dinnebier, C. R. Ast, M. Burghard, K. Kern, *Nano Lett.* **2013**, *13*, 1179.
[30] B. G. Weissberg, *Am. Mineral.* **1965**, *50*, 1817.
[31] P. Wang, D. He, J. He, J. Fu, S. Liu, X. Han, Y. Wang, H. Zhao, *J. Phys. Chem.* **2020**, *124*, 1047.
[32] T. Guillermo, B. Wuensch, *Acta Crystallogr., Sect. B: Struct. Sci., Cryst. Eng. Mater.* **1973**, *29*, 2536.
[33] A. Kyono, M. Kimata, *Am. Mineral.* **2004**, *89*, 696.
[34] M. Velický, P. S. Toth, A. M. Rakowski, A. P. Rooney, A. Kozikov, C. R. Woods, A. Mishchenko, L. Fumagalli, J. Yin, V. Zólyomi, *Nat. Commun.* **2017**, *8*, 14410.
[35] C. Razzetti, P. Lottici, *Solid State Commun.* **1979**, *29*, 361.
[36] R. Parize, T. Cossuet, O. Chaix-Pluchery, H. Roussel, E. Appert, V. Consonni, *Mater. Des.* **2017**, *121*, 1.
[37] L. Li, W. Wang, P. Gong, X. Zhu, B. Deng, X. Shi, G. Gao, H. Li, T. Zhai, *Adv. Mater.* **2018**, *30*, 1706771.
[38] N. Youngblood, R. Peng, A. Nemilentsau, T. Low, M. Li, *ACS Photonics* **2017**, *4*, 8.
[39] A. Dasgupta, J. Gao, X. Yang, *Laser Photonics Rev.* **2020**, *14*, 1900416.
[40] H. Sar, J. Gao, X. Yang, *Sci. Rep.* **2020**, *10*, 14282.
[41] J. Yu, X. Kuang, Y. Gao, Y. Wang, K. Chen, Z. Ding, J. Liu, C. Cong, J. He, Z. Liu, Y. Liu, *Nano Lett.* **2020**, *20*, 1172.
[42] J. Wu, X. Cong, S. Niu, F. Liu, H. Zhao, Z. Du, J. Ravichandran, P. H. Tan, H. Wang, *Adv. Mater.* **2019**, *31*, 1902118.
[43] H. Yang, H. Jussila, A. Autere, H.-P. Komsa, G. Ye, X. Chen, T. Hasan, Z. Sun, *ACS Photonics* **2017**, *4*, 3023.
[44] Y. Yang, S. C. Liu, Y. Wang, M. Long, C. M. Dai, S. Chen, B. Zhang, Z. Sun, Z. Sun, C. Hu, *Adv. Opt. Mater.* **2019**, *7*, 1801311.
[45] X. L. Yang, S. W. Xie, *Appl. Opt.* **1995**, *34*, 6130.
[46] R. W. Boyd, *Nonlinear Optics*, Academic Press, Cambridge MA **2020**.
[47] M. Fleischer, J. J. Matzko, R. E. Wilcox, *Microscopic Determination of the Nonopaque Minerals*, US Government Printing Office, Washington, D.C. **1984**.